



## Article

# Analysis of Atmospheric Boundary Layer Characteristics on Different Underlying Surfaces of the Eastern Tibetan Plateau in Summer

Xiaohang Wen <sup>1,2</sup> , Jie Ma <sup>3,\*</sup> and Mei Chen <sup>1</sup>

<sup>1</sup> Plateau Atmosphere and Environment Key Laboratory of Sichuan Province, College of Atmospheric Sciences, Chengdu University of Information Technology, Chengdu 610225, China; wxh@cuit.edu.cn (X.W.); 3220101022@stu.cuit.edu.cn (M.C.)

<sup>2</sup> State Key Laboratory of Severe Weather, Chinese Academy of Meteorological Sciences, Beijing 100081, China

<sup>3</sup> Luzhou Meteorological Bureau, Luzhou 646099, China

\* Correspondence: mjie9@hotmail.com

**Abstract:** The atmospheric boundary layer is a key region for human activities and the interaction of various layers and is an important channel for the transportation of momentum, heat, and various substances between the free atmosphere and the surface, which has a significant impact on the development of weather and climate change. During the Second Tibetan Plateau Scientific Expedition and Research Program (STEP) in June 2022, utilizing the comprehensive stereoscopic observation experiment of the “Plateau Low Vortex Network”, this study analyzed the variation characteristics and influencing factors of the atmospheric boundary layer height (ABLH) at three stations with different underlying surface types on the Qinghai–Tibet Plateau (QTP): Qumalai Station (grassland), Southeast Tibet Observation and Research Station for the Alpine Environment (SETORS, forest), and Sieshan Station (cropland). The analysis utilized sounding observation data, microwave radiometer data, and ERA5 reanalysis data. The results revealed that the temperature differences between the sounding observation data and microwave radiometer data were minor at the three stations, with a notable temperature inversion phenomenon observed at Sieshan Station. Regarding water vapor density, the differences between the sounding observation data and microwave radiometer data were relatively small at Sieshan Station. The relative humidity increased with height at Sieshan Station, whereas it increased and then decreased with height at SETORS and Qumalai Station. The ABLH at all sites reached its maximum value around noon, approximately 1500 m, and exhibited mostly convective boundary layer (CBL) characteristics. During the night, the ABLH mostly showed a stable boundary layer (SBL) pattern, with heights around 250 m. In summer, latent heat flux (LE) and sensible heat flux (H) in the eastern plateau were generally lower than those in the western plateau except at 20:00, where they were higher. Vertical velocity ( $w$ ) in the eastern plateau was greater than in the western plateau. Among Sieshan Station and SETORS, LE, and H had the most significant impact on ABLH, while at Qumalai Station, ABLH was more influenced by surface long-wave radiation ( $R_{lu}$ ). These four influencing factors showed a positive correlation with ABLH. The impact of different underlying surface types on ABLH primarily manifests in surface temperature variations, solar radiation intensity, vegetation cover, and terrain. Grasslands typically exhibit a larger range of ABLH variations, while the ABLH in forests and mountainous cropland areas is relatively stable.

**Keywords:** Tibetan Plateau; atmospheric boundary layer; different underlying surfaces; ERA5; impact factors



**Citation:** Wen, X.; Ma, J.; Chen, M. Analysis of Atmospheric Boundary Layer Characteristics on Different Underlying Surfaces of the Eastern Tibetan Plateau in Summer. *Remote Sens.* **2024**, *16*, 1645. <https://doi.org/10.3390/rs16091645>

Academic Editor: Carmine Serio

Received: 2 April 2024

Revised: 24 April 2024

Accepted: 2 May 2024

Published: 5 May 2024



**Copyright:** © 2024 by the authors. Licensee MDPI, Basel, Switzerland. This article is an open access article distributed under the terms and conditions of the Creative Commons Attribution (CC BY) license (<https://creativecommons.org/licenses/by/4.0/>).

## 1. Introduction

The atmospheric boundary layer (ABL), or planetary boundary layer (PBL), is the part of the troposphere that is directly influenced by the ground, and it responds to the

action of the ground on a time scale of 1 h or less, up to a height of several kilometers. It is an important channel for the transport of momentum, heat, and various materials in the Earth's atmosphere and has an important role in the exchange of energy and materials between the Earth's surface and the free atmosphere [1–4]. A deeper understanding of the structure and characteristics of the ABL will help to better understand the transfer and circulation of energy and matter in the Earth system [5–9]. The average altitude of the TP is above 4 km, and the plateau has a unique ABL formed by strong solar radiation, a significant temperature difference between the ground and the complex topography [8,10,11]. The interplay between the eastern plateau's intricate topography and diverse circulation systems contributes to unique weather and climate features in the region. Therefore, it is important to study the ABL structure in this region to understand the genesis of weather and climate and its influence on the weather in China [11,12].

Based on the important research value of the ABL on the TP, many scholars have conducted a lot of research on the Atmospheric Boundary Layer height (ABLH) and the vertical distribution of meteorological elements in the boundary layer on the TP in recent decades. Li et al. [13–15] found that the height of the convective mixed layer in the northern TP is higher in the dry season than in the rainy season, and the specific humidity in the dry season is smaller than that in the wet season. The convective ABL is formed later on rainy days than on cloudy and sunny days. And glacial winds affect the ABLH in the Everest region with a maximum height of 3888 m. Su et al. [1] found that the main influencing factors of ABLH in the western region are 0–10 cm soil water content and 10 m wind speed, while the main influencing factor of ABLH in the eastern region is cloudiness. It has been shown that the ABLH in the plateau under the south branch of the westerly wind field is higher than that under the summer wind field in the plateau [8]. Ma et al. [16] used radio sounding data to find that the temperature decreases at a rate of 0.74 K/100 m in the summer in the northern TP, and the relative humidity increases and then decreases with height. Gu et al. [17] found that inversion humidity occurred in the summer in both the Amdo and Nagqu regions, with strong inversion humidity mainly occurring at midnight or midday. Wang and Ma [18] studied the ABL structure in the Everest region and found that the wind speed in summer varies greatly from day to day, especially in the afternoon, and the wind speed increases with height at about 1800–2300 m and then decreases upward. height. Chen et al. [19] found that the winter ABL in the western TP can reach up to 9.2 km above sea level, which is close to the height of the top of the troposphere in the plateau region. Xu et al. [9] found that the mean ABLH in the eastern and downstream areas of the plateau is high during the day and low at night, while the mean ABLH in the central part of the plateau is lower around sunrise and then gradually increases with time.

The above studies have investigated the ABL of the TP from various aspects, including the ABLH, the vertical trends of meteorological elements within the boundary layer, and the factors affecting the development of ABLH, which are important for further understanding the structure and characteristics of ABL on the plateau. However, these studies mostly focus on a single underlying surface, and the comparative analysis of ABL characteristics in different underlying surfaces is less. This study compares and analyzes the sounding observations and ERA5 reanalysis data from the Qumalai and SETORS stations located in the eastern part of the plateau and the Sieshan station located at the southeastern edge of the plateau in June 2022 and combines them with the microwave radiometer data from the Sieshan station, to study the characteristics of ABL in the different underlying surfaces in the eastern part of the plateau and the factors influencing ABLH, which can help to understand the process and structure of the atmospheric boundary layer in the area and to provide some references for the study on the development of the weather and the climate change.

## 2. Data and Methods

### 2.1. Data

#### 2.1.1. Observation Data

The three stations in this paper are as follows: Sieshan station is located on the southeastern edge of the TP (Figure 1). Its underlying surface is dominated by farmland and its altitude is 807 m (Table 1). SETORS is located in the southeast of the TP (Figure 1), and its underlying surface is dominated by evergreen needleleaf forests, with an altitude of 3327 m (Table 1). Qumalai station is located in the eastern TP. Its underlying surface is mainly grassland, and its altitude is 4199 m (Table 1).

**Table 1.** Description of geographic features of three sites.

Station	Latitude	Longitude	Elevation (m)	Land Cover
Qumalai	34.13°N	95.81°E	4199	grassland
SETORS	29.75°N	94.75°E	3327	evergreen needleleaf forests
Sieshan	29.27°N	103.60°N	807	farmland

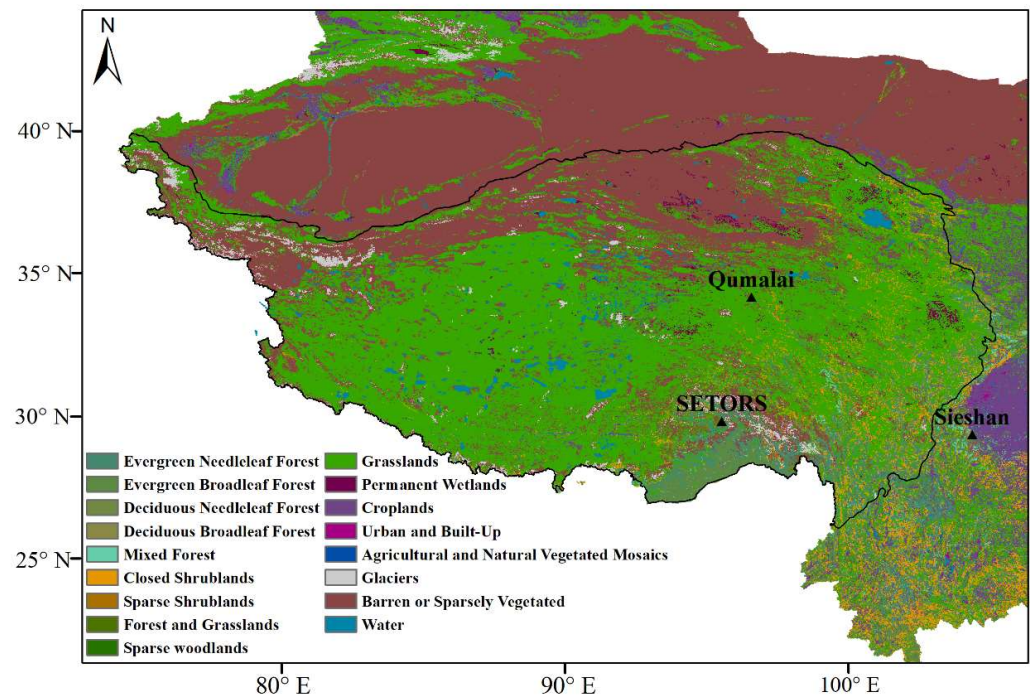
In this study, sounding data from three stations (Qumalai station, SETORS, and Sieshan station) of the Second Tibetan Plateau Scientific Expedition and Research on the TP were used from June 10 to 18 and 26 to 30. The Qumalai station uses the RS92 sounding instrument of Vaisala company, which collects and sends a set of data of pressure, temperature, humidity, wind speed and wind direction per second, among which the range of atmospheric pressure measurement is 1080 to 3 hPa, the resolution is 0.4 hPa when it is larger than 100 hPa, and 0.3 hPa when it is smaller than 100 hPa, and the combined uncertainty is 1.0 hPa when it is larger than 100 hPa in the sounding. The measurement range of the temperature sensor is  $-90$ – $60$  °C, the resolution is 0.2 °C, and the combined uncertainty is 0.5 °C in the sounding. The measurement range of the humidity sensor is 0–100%RH with a resolution of 2%RH, and the combined uncertainty is 5%RH in the sounding. The wind speed is measured with a resolution of 1 m/s, and the combined uncertainty is 0.15 m/s in the sounding (Table 2) [20]. And the Sieshan station and SETORS use an RS41-SG type sounding instrument; it is the latest generation of Vaisala company full digital sounding instrument that collects and sends a set of pressure, temperature, humidity, wind speed, and wind direction every second, including atmospheric pressure measurement range for the surface pressure to 3 hPa, the resolution is 0.01 hPa, the combined uncertainty in the sounding is 1.0 hPa when it is greater than 100 hPa, 0.3 hPa when it is between 100 and 10 hPa, and 0.04 hPa when it is less than 10 hPa. The temperature sensor measurement range is  $-95$ – $60$  °C, the resolution is 0.01 °C, the combined uncertainty is 0.3 °C when the height is less than 16 km and 0.4 °C when the height is more than 16 km in the sounding. The measurement range of the humidity sensor is 0–100%RH, the resolution is 0.1%RH, and the combined uncertainty is 4%RH in the sounding. Wind speed resolution is 0.1 m/s, and the combined uncertainty is 0.15 m/s. The wind direction measurement range is 0–360°, the resolution is 0.1°, and the combined uncertainty is 2° (Table 3).

**Table 2.** RS92 sounding instrument main performance.

Projects	Atmospheric Pressure (hPa)	Temperature (°C)	Humidity (%RH)	Wind Speed (m/s)
Measurement Range	1080 to 3	$-90$ – $60$	0–100	/
Resolution	0.4 (>100)	0.2	2	1
	0.3 (<100)			
combined uncertainty	1.0 (>100)	0.5	5	0.15
	0.6 (<100)			
	0.6 (<10)			

**Table 3.** RS41-SG sounding instrument main performance.

Projects	Atmospheric Pressure (hPa)	Temperature (°C)	Humidity (%RH)	Wind Speed (m/s)	Wind Direction (°)
Measurement Range	surface pressure-3	−95–60	0–100	/	0–360
Resolution	0.01	0.01	0.1	0.1	0.1
combined uncertainty	1.0 (>100)	0.3 (<16 km)	4	0.15	2
	0.3 (<100)	0.4 (>16 km)			
	0.04 (<10)				

**Figure 1.** Spatial pattern of land use and station distribution [21].

### 2.1.2. Microwave Radiometer Data

In this study, the microwave radiometer model MWP967KV is used to automatically invert atmospheric temperature, humidity, cloud water distribution, water vapor, liquid water content, and other atmospheric parameters in the headspace in real time, and can continuously detect the temperature (°C), water vapor density ( $\text{g}/\text{m}^3$ ), relative humidity (%) and liquid water content ( $\text{g}/\text{m}^3$ ) from the ground to an altitude of 10,000 m. MWP967KV observation: one layer every 25 m below 500 m, one layer every 100 m from 500 m to 2000 m, and one layer every 250 m from 2000 m to 10,000 m, for a total of 83 layers. Each layer includes temperature, water vapor density, relative humidity, and liquid water content and returns a set of data every 2 min. Since the ABL is mainly studied in this paper, only data below 5000 m are used, and interpolation is carried out on the data to make the vertical resolution below 5000 m become 10 m to compare and analyze with the observation data.

### 2.1.3. ERA5 Reanalysis Data

The ERA5 [22] reanalysis data are the fifth generation of atmospheric reanalysis data for global climate from the ECMWF (European Centre for Medium-Range Weather Forecasts). The reanalysis data combine model data with observations from around the world to form a globally complete and consistent dataset. ERA5 is generated from 4D-Var data assimilation and model forecasts in CY41R2 of the ECMWF Integrated Forecast System (IFS) and also provides “surface or single level” data containing 2D parameters such as

precipitation, top-of-atmosphere radiation, and vertical integrals over the entire depth of the atmosphere, while parameters such as 2 m temperature and soil temperatures are generated by coupling the atmospheric model in IFS with a land-surface model (HTESSEL). The time coverage ranges from 1950 to now. The time resolution is 1 h, and the spatial resolution is  $0.25^\circ \times 0.25^\circ$ . In this study, the data used are the hourly vertical velocity and hourly LE, H, Rlu, and ABLH data of ERA5 reanalysis data in June 2022.

## 2.2. Analysis Method

### 2.2.1. Calculation Method of ABLH

In this paper, for the convenience of analysis and comparison, the sounding data of the three sites are uniformly processed into a vertical resolution of 10 m. The ABL is divided into a convective boundary layer and a stable boundary layer for analysis, and this division is based on the potential temperature profile and Richardson number (Ri) profile to discriminate [23]. The ABLH was estimated by the gas block method and Ri method, respectively. The Ri can be calculated using the following formula [24]:

$$Ri(z) = \frac{g(z - z_0) \theta_v(z) - \theta_v(z_0)}{\theta_v(z) u(z)^2 + v(z)^2} \quad (1)$$

$$u(z) = V(z) \sin \alpha(z) \quad (2)$$

$$v(z) = V(z) \cos \alpha(z) \quad (3)$$

where  $g$  is the acceleration of gravity, taken as  $9.81 \text{ m/s}^2$ ,  $z_0$  is the ground elevation,  $\theta_v$  is the imaginary temperature, while  $u$  and  $v$  are the latitudinal and longitudinal wind components, respectively,  $V$  is the wind speed, and  $\alpha$  is the wind direction.

The formula for calculating the virtual potential temperature ( $\theta_v$ ) is as follows:

$$r_s = \frac{\varepsilon e_s}{P} \quad (4)$$

$$t \geq 0, e_s = 6.112 e^{\left(\frac{17.67t}{t+243.5}\right)}; t < 0, e_s = 6.1078 * 10^{\left(\frac{7.5t}{t+237.3}\right)} \quad (5)$$

$$U_w = \frac{r_s}{r} \quad (6)$$

$$\theta_v = \theta(1 + 0.608r) \quad (7)$$

In the above equation  $r_s$  is the saturation mixing ratio,  $\varepsilon \approx 0.622$ ,  $e_s$  is the saturation vapor pressure,  $t$  is the Celsius temperature,  $U_w$  is the relative humidity,  $r$  is the mixing ratio,  $P$  is the atmospheric pressure, and  $\theta$  is the potential temperature [25].

The boundary layer height is discriminated as follows:

$$\theta_{200} - \theta_0 < 0, R_i(0 \sim 100) < 0 \text{ i.e. } \theta_v(100) - \theta_v(0) < 0 \text{ CBL; else SBL} \quad (8)$$

where  $\theta_{200}$  and  $\theta_0$  represent the potential temperature at 200 m and at ground level, respectively, and  $\theta_v(100)$  and  $\theta_v(0)$  represent the virtual potential temperature at 100 m and at ground level, respectively [25].

The relative maximum value  $\theta_{v0}$  of the virtual potential temperature  $\theta_v$  on the ground, rises vertically until the height of  $\theta_{v0}$  is detected again, and we define this height as the ABLH and this method is referred to as the air-block method [26], as shown in Figure 2. When the ABL is a convective boundary layer (CBL) structure, the gas block method is used to determine the ABLH [9,23–25,27].

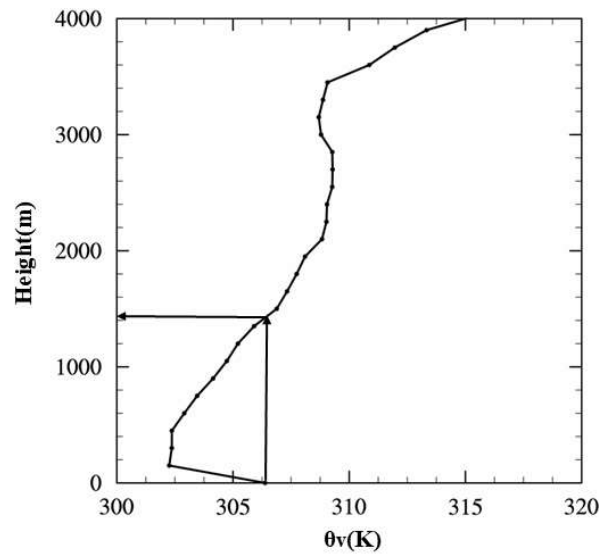


**Figure 2.** Schematic diagram of CBL height determination by the gas block method.

When the ABL is a stable boundary layer (SBL) structure, the Ri method is usually used to estimate the ABLH. The SBL height is defined as the height where the Ri is equal to or greater than a pre-given critical value [28]. In this study, the critical Richardson number (Ric) is used as a common value Ric = 0.25 [29].

### 2.2.2. Water Vapor Density ( $\rho_v$ ) Calculation

$$q = \frac{\varepsilon e}{p} \quad (9)$$

$$\rho_v = \frac{\varepsilon e}{R_d T} \quad (10)$$

where  $e$  is the actual water vapor pressure,  $q$  is the specific humidity,  $\rho_v$  is the water vapor density,  $R_d$  is the specific gas constant of air, which is  $287 \text{ J}\cdot\text{K}^{-1}\cdot\text{Kg}^{-1}$ , and  $T$  is the Kelvin temperature.

### 2.2.3. Correlation Coefficient (R) Calculation

R is a statistical indicator that reflects the closeness of the correlation between the variables. The value of R is between  $-1$  and  $1$ . If the coefficient is positive then the two variables are positively correlated. If the coefficient is negative then the correlation is negative. The greater the absolute value, the stronger the correlation.

$$R = \frac{\sum_{i=1}^n (x_i - \bar{x})(y_i - \bar{y})}{\sqrt{\sum_{i=1}^n (x_i - \bar{x})^2 \sum_{i=1}^n (y_i - \bar{y})^2}} \quad (11)$$

where  $y_i$  is the ERA5 reanalysis data for each variable,  $x_i$  is the ABLH, and  $n$  is the number of samples.

## 3. Results and Analysis

### 3.1. Analysis of ABL Characteristics

#### 3.1.1. Vertical Variation Characteristics of Meteorological Elements in the ABL

Figure 3 shows the comparison of average temperature and vertical distribution characteristics of water vapor density between the microwave radiometer and observation data at Sieshan station. It can be seen from the figure that the temperature changes regularly at four times, and the difference between the two data is not obvious. However, it can be seen from Figure 3a that the temperature at 02:00 at the lower level is significantly higher

than that at the other three times. However, there is no significant difference between the four times in Figure 3b, and compared with the microwave radiometer data (Figure 3a), there is an obvious temperature inversion in the lower layer. As for the water vapor density, there is a large difference between the four times of the microwave radiometer data. It can be seen from Figure 3c that the water vapor density is the highest at 02:00 below 2800 m and the lowest at 08:00 within 1000–3600 m. Different from Figure 3c, there is no significant difference in the variation of water vapor density at the four times in Figure 3d, but the water vapor density at 14:00 within 1000 m to 3600 m is slightly lower than the other three times.

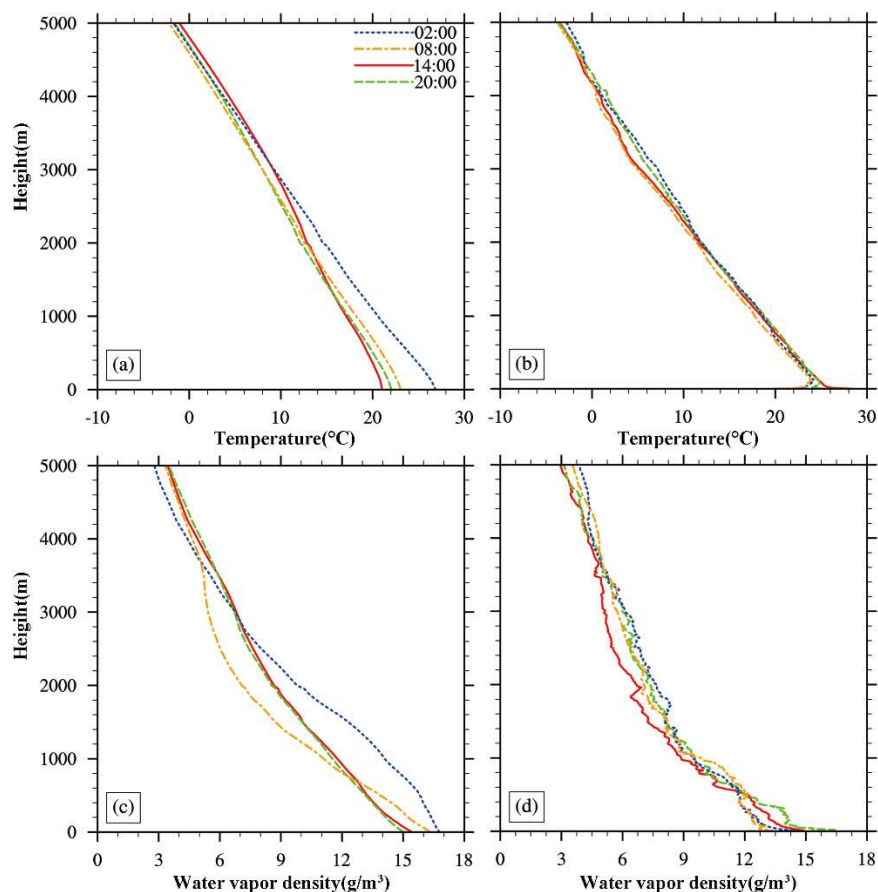


**Figure 3.** The vertical distribution characteristics of mean temperature and water vapor density of microwave radiometer data (a,c) and observation data (b,d) at Sieshan station (The 4 subfigures of a–d share a common legend).

The vertical structure of the thermal and dynamic properties of the ABL has a significant effect on the transport and distribution of material within it [30], and the distribution of water vapor in the vertical direction is then influenced by the turbulent action within the ABL. Figure 4 shows the characteristics of the vertical distribution of relative humidity and specific humidity at the three stations, from which it can be seen that the vertical variation of relative humidity at Sieshan station below 5000 m increases gradually with height, while the relative humidity at SETORS decreases and then increases and then decreases with height, and the relative humidity at Qumalai station increases and then decreases with height (Figure 4a–c). The relative humidity at 1400–3000 m is smaller than at other times, while the relative humidity at 08:00 is larger than at other times at every level of height, indicating that the ABL is richer in water vapor at 08:00 in Sieshan station (Figure 4a). The vertical variation of relative humidity at 14:00 in SETORS is different from the other moments, with the surface relative humidity smaller than the other moments then gradually increasing and then decreasing. The relative humidity first decreases slightly from the surface and

then increases at the other three moments. The relative humidity at SETORS reaches a maximum of around 2000 m, close to 100%, and then gradually decreases (Figure 4b). The relative humidity at Qumalai station also reached a maximum around 2000 m, close to 90%. The relative humidity at the Qumalai station did not change significantly below 2000 m at 08:00, and the surface relative humidity at 14:00 and 20:00 was the smallest among the three stations (Figure 4c).

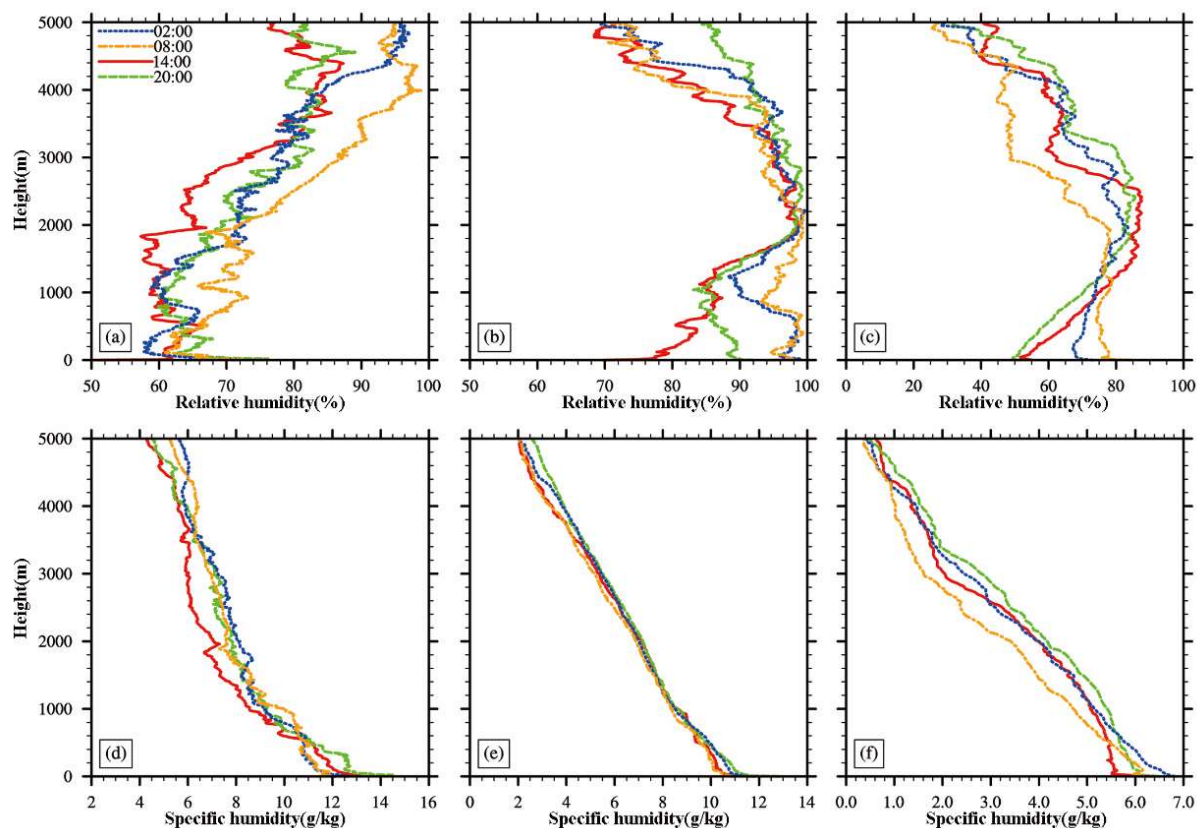


**Figure 4.** Vertical distribution characteristics of mean relative humidity and specific humidity at Sieshan stations (a,d), SETORS (b,e), and Qumalai station (c,f) (The 6 subfigures of a–f share a common legend).

Specific humidity is also an important parameter to characterize the distribution of water vapor in the vertical direction. As can be seen from the figure, the specific humidity of the near-surface layer is the smallest at Qumalai station, followed by SETORS, and the largest at Sieshan station (Figure 4d–f), which may be related to the geographical location, altitude, and ground heating field. The inverse humidity appears near the ground at 08:00 at Qumalai station (Figure 4f). The inverse temperature in the SBL and near the top of the CBL, low-level jet on water vapor transport, etc. These may form the inverse humidity within the near-ground layer [8].

Wind is one of the main meteorological elements of the energy and material transport exchange process in the ABL. Figure 5 shows the vertical distribution characteristics of wind direction and wind speed at the three stations. In addition to the 14:00 ground wind direction at Sieshan station, which is mainly easterly, the other wind directions are mainly southwesterly, and the wind direction at 1000–2000 m altitude is mainly southeasterly, and the wind direction above 2000 m gradually turns to southerly or southwesterly (Figure 5a). The wind direction below 1000 m varies greatly from day to day at SETORS, with easterly winds dominating at 14:00, southeasterly winds at 08:00 and 20:00, and southerly winds at 02:00. The wind direction above 1200 m changed less noticeably daily at SETORS, and the wind direction gradually changed to southerly or southwesterly (Figure 5b). Below 1800 m

at Qumalai station, southeasterly winds predominate, while above 1800 m, they gradually change to southwesterly or westerly winds (Figure 5c).

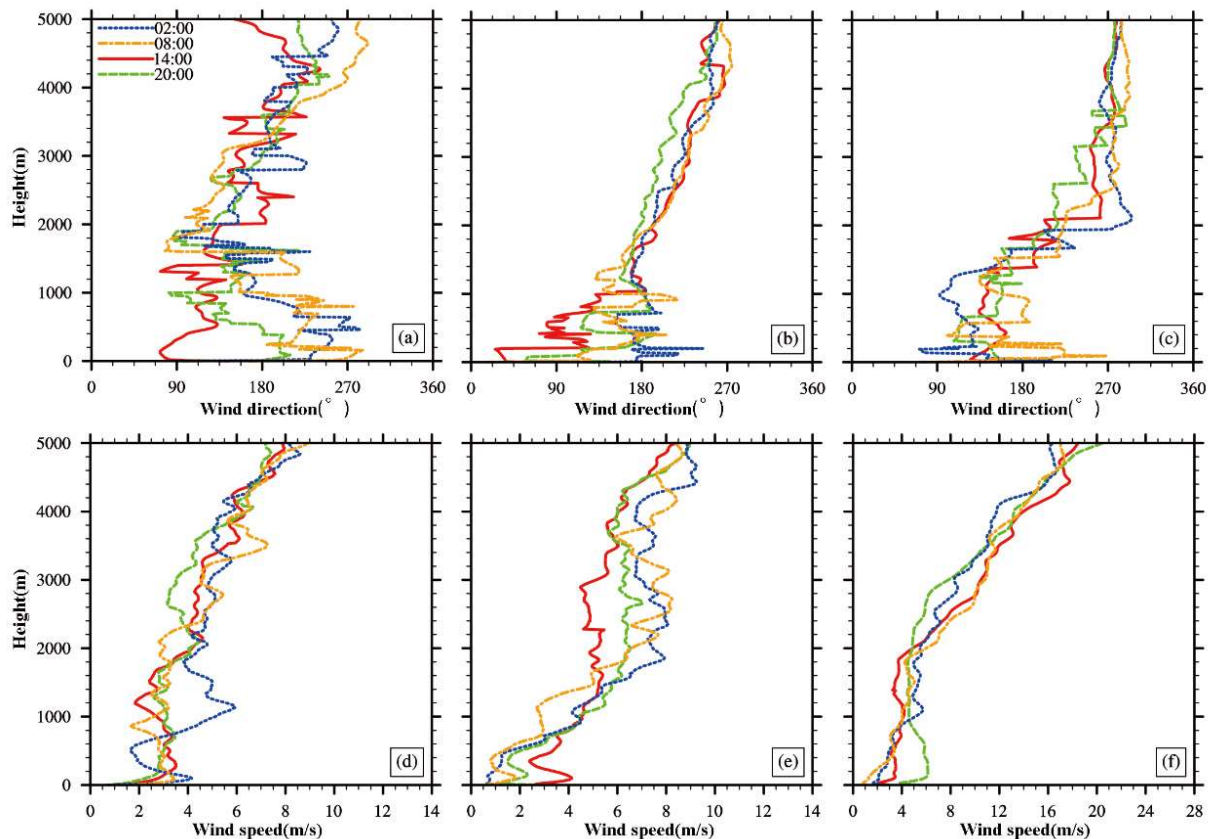


**Figure 5.** Vertical distribution characteristics of mean wind direction and wind speed at Sieshan stations (a,d), SETORS (b,e), and Qumalai station (c,f) (The 6 subfigures of a–f share a common legend).

Among the three stations, the wind speed at Qumalai station varied greatly with height, with a maximum wind speed of 20 m/s (Figure 5f). The wind speed varied less with height at Sieshan station, and the maximum wind speed could reach 9 m/s (Figure 5d). There was a sharp decrease in wind speed at 100 m at 02:00, and then, the wind speed started to increase sharply at 500 m and started to decrease at 1200 m (Figure 5d). At SETORS, except for 02:00, there was a sharp decrease in wind speed at 100 m, and then the wind speed increased sharply at 400 m, and the wind speed increased slowly with height above 1600 m at 14:00 (Figure 5e). At 20:00, the ground wind speed at Qumalai station reached a maximum of 4 m/s, and the wind speed began to increase sharply above 3000 m. At 02:00, 08:00, and 14:00, the wind speed increased sharply to around 2000 m, and the maximum wind speed was 20 m/s, which is the largest among the three stations (Figure 5f).

### 3.1.2. The ABLH Characteristics

Figure 6 shows the change process of the average ABLH at the three stations for four time periods, and it can be seen from the figure that the ABLH of each station reaches the maximum at 14:00. Combined with Figure 7a, the ABL type at night is mostly SBL at Sieshan station, and the ABLH is around 250 m (Figure 6). At 08:00, the ABLH type is SBL; it is mostly CBL at 14:00, and the ABLH can reach 1400 m during the day. The diurnal variation of the ABLH at SETORS and Sieshan station is similar. At 14:00, the ABLH at SETORS is slightly lower than that at Sieshan station, while the ABLH at SETORS is higher than that at Sieshan station at night (Figure 6). The ABL type at SETORS is mainly CBL at night (Figure 7b), and the frequency of both types of boundary layers is the same at 02:00,

while the ABL is mainly CBL at 20:00 and also mainly CBL during the day (Figure 7b), which indicates that convection is developing vigorously and there is relatively strong convective activity even at night at SETORS, which may be related to the underlying surface and surface heating field. The ABLH is the highest among the three stations at 14:00 in Qumalai station, reaching about 1500 m. By 20:00, the ABLH is still high; compared with 14:00, it only decreases about 100 m (Figure 6), and combined with Figure 7c, we can see that the ABL type is dominated by CBL at 14:00 and 20:00, indicating that the convective activity in the afternoon continues into the evening for a longer time at Qumalai station. The ABLH is lower at 02:00 and 08:00, and the ABLH at 08:00 is significantly lower than that at 02:00 (Figure 6). Combined with Figure 7c, there are SBL at 02:00 and 08:00, indicating that the ABL is more stable during this period, and no convective activity is generated, or only weak convection is present during this period. The ABLH is the highest at Qumalai station among the three stations during the day, around 750 m and 800 m, respectively (Figure 6).

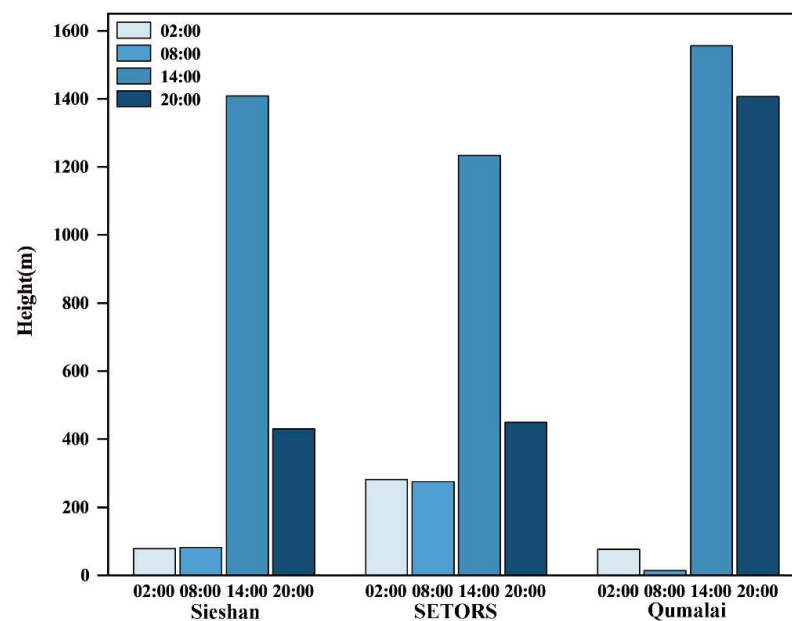


Figure 6. Diurnal variation of mean ABLH at three stations.

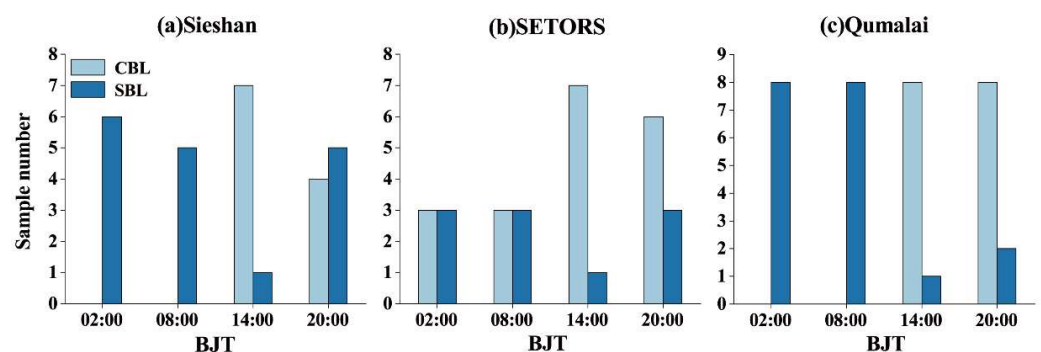
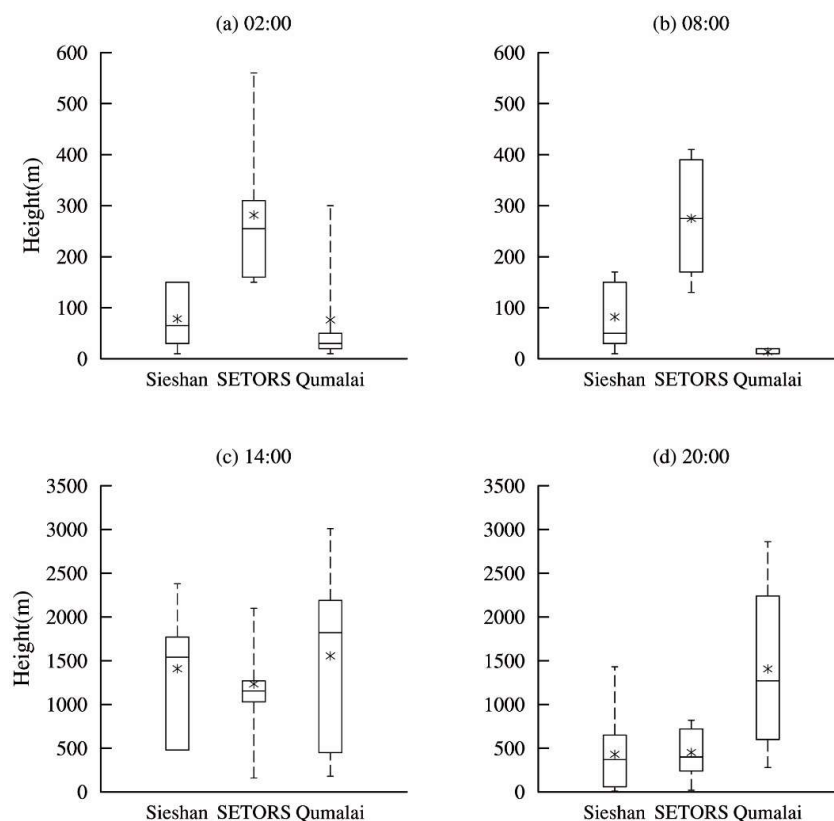


Figure 7. Diurnal variation of sample numbers of CBL and SBL at three stations (The 3 subfigures of a–c share a common legend).

Figure 8 shows the box plot of ABLH at each station for four time periods. It can be seen from the figure that the ABLH of the three stations varies greatly at different times. At 02:00 (Figure 8a), the ABLH is the highest compared with the other two stations at SETORS, mainly around 150–400 m. The ABLH is below 200 m at Sieshan station, while that is mainly below 100 m at Qumalai station. At 08:00 (Figure 8b), the ABLH at each station is

similar to that at 02:00, with the ABLH at Qumalai station becoming significantly lower compared to that at 02:00, while the ABLH at SETORS is mostly slightly higher than that at 02:00. At 14:00 (Figure 8c), the ABLH is mainly below 2000 m at Sieshan station, and the ABLH is mainly around 1000–1500 m at SETORS, while ABLH is mainly below 2500 m at Qumalai station, and the ABLH varied within 500–2300 m, with a large range of variation. Except the ABLH slightly decreases at Qumalai station, the ABLH decreases significantly at the other two stations, and the ABLH mostly decreases to below 1000 m at these two stations. Compared with the ABLH at 20:00 and 02:00, the ABLH decreases sharply at Qumalai station, which indicates that the convective activity is strong during the day and weak at night at Qumalai station. The daily variation of ABLH is the smallest at SETORS.



**Figure 8.** Box plot of ABLH at three stations, the \* indicates outliers.

In general, the factors influencing the height of the atmospheric boundary layer include Topography: The height and complexity of the terrain affect the development and ABLH. For example, rugged mountainous areas often result in lower atmospheric boundary layer heights, while flat areas may have higher atmospheric boundary layer heights. Surface Temperature: Variations in surface temperature directly impact the height of the atmospheric boundary layer. Warmer surface temperatures during the day increase the atmospheric boundary layer height, while cooler surface temperatures at night decrease it. Solar Radiation: The intensity and distribution of solar radiation also influence changes in the height of the atmospheric boundary layer. Regions with intense radiation typically have higher atmospheric boundary layer heights. Vertical velocity and Horizontal Wind: Vertical velocity and horizontal wind in the atmosphere significantly affect the height of the atmospheric boundary layer. Upward velocity increases the boundary layer height, while downward velocity decreases it. Surface Features: Surface features, including vegetation cover and water distribution, also affect the height of the atmospheric boundary layer. Dense vegetation areas typically have lower ABLH.

The three representative sites selected in this study represent alpine grassland, forests, and mountainous cropland areas. Qumalai Station, located in the hinterland of the QTP,

has flat terrain. Influenced by intense daytime surface heating, vigorous vertical convection develops, increasing the surface sensible heat flux and the temperature gradient in the atmospheric boundary layer. This gradient promotes the development of convection, resulting in the highest boundary layer height among the three stations, which can be sustained until evening. The cooling effect from nighttime surface radiation is evident, leading to the lowest boundary layer height. SETORS Station has a forested underlying surface, resulting in the lowest atmospheric boundary layer height among the three stations during the day. This is due to the dense vegetation reducing direct solar energy reaching the surface, which lowers the surface temperature and limits the upward extent of the atmospheric boundary layer. Additionally, the dense vegetation increases surface roughness, reducing wind speeds within the canopy layer and slowing vertical diffusion, contributing to the lower boundary layer height. Sieshan Station is situated in a lower-altitude mountainous cropland area with less intense solar radiation and less dense vegetation compared to SETORS station. This results in a moderate increase in surface temperature and an atmospheric boundary layer height between that of forests and grasslands.

### 3.2. Analysis of Factors Influencing the ABLH

#### 3.2.1. Comparison of ABLH between Observed Data and ERA5 Reanalysis Data

Figure 9 shows the hourly variation of mean ABLH between the ERA5 reanalysis data and the observed data in June, from which it can be seen that the hourly variation of ABLH at the three stations is basically the same. The ABLH is lower in the morning and evening and reaches the highest at 15:00, among which the ABLH is the highest at Qumalai station, followed by the SETORS and finally the Sieshan station. At 02:00, the ABLH of ERA5 reanalysis data is smaller than that of observed data at SETORS and Sieshan station, while the opposite is true at Qumalai station. At 08:00, the ABLH of ERA5 reanalysis data is still smaller than that of the observed data at SETORS, while the ABLH of ERA5 reanalysis data is larger than that of the observed data at Qumalai station. At 14:00, the ERA5 reanalysis data of both SETORS and the Sieshan station show significant overestimation of the observed data, while at 20:00, the Sieshan and Qumalai stations show significant underestimation. In summary, the ABLH of ERA5 reanalysis data is smaller than that of the observed data in the morning and evening at Sieshan station and SETORS, and the opposite is true at noon. The ABLH of ERA5 reanalysis data is larger than that of the observed data in the morning and evening, and the difference between them is not obvious at noon in Qumalai station.

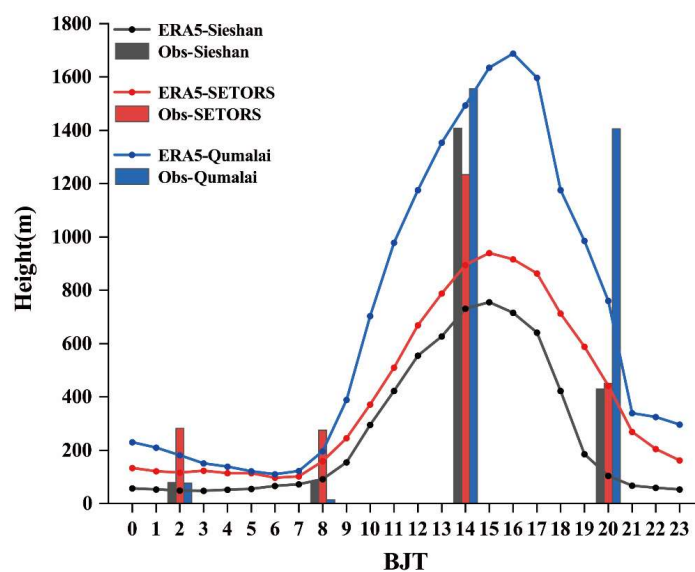
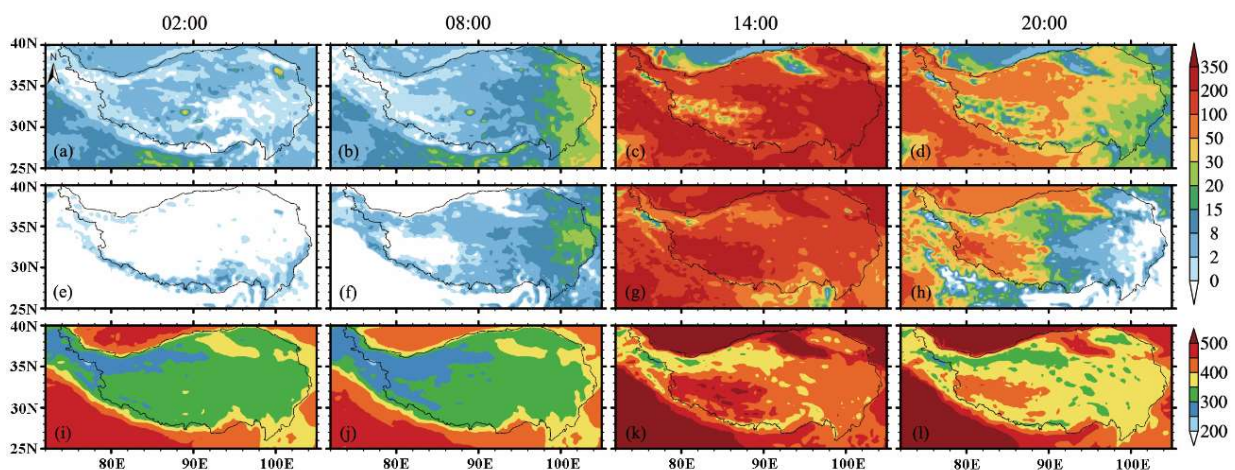


**Figure 9.** Hourly variation of the mean ABLH between the ERA5 reanalysis data and the observed data in June.

### 3.2.2. Spatial Distribution Characteristics of the Surface Heating Field (Latent Heat Flux (LE) and Sensible Heat Flux (H)), Surface Long-Wave Radiation (Rlu), and Vertical Velocity (w) in Four Time Periods

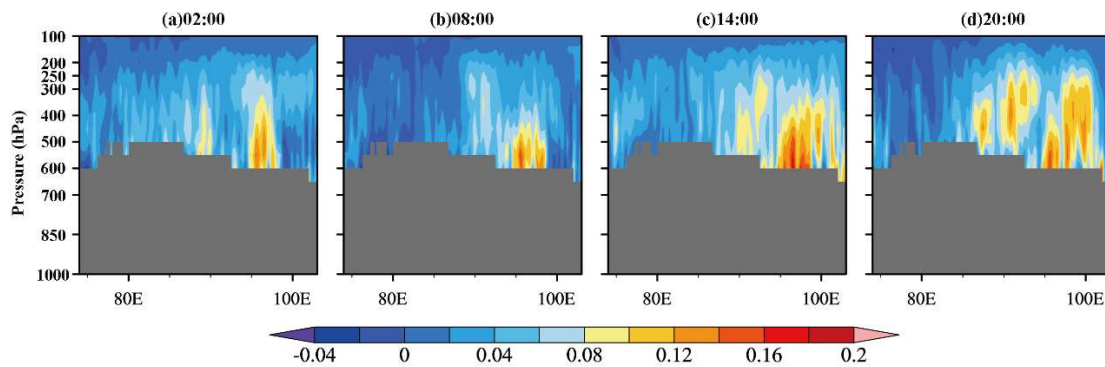
The H is the heat transport between the surface and atmosphere caused by turbulent motion near the ground, and LE is the heat transport between the surface and atmosphere caused by the phase change in water in the atmosphere. Therefore, H and LE are the key physical quantities that influence the formation and development of the atmospheric thermal boundary layer [10].

Figure 10 shows the spatial distribution characteristics of the surface heating field (LE and H), Rlu, and w in four time periods on the TP. In summer, the surface heating field of the plateau is dominated by LE. From 02:00 to 14:00, the heating of the surface by solar radiation gradually increases, and the LE and H increase. The LE and H are always larger in the eastern plateau than in the western plateau due to different underlying surfaces and altitudes (Figure 10a–c,e–g). At 20:00, the intensity of the surface heating field gradually decreases, and the LE and H in the western plateau are larger than those in the eastern plateau (Figure 10d,h), which indicates that during the period of gradual heating of the surface by solar radiation, the eastern plateau absorbs energy faster and exchanges energy faster, and the intensity of surface heating field rapidly decreases when there is no solar radiation heating. At 02:00 and 08:00, the Rlu value in the western plateau is smaller than that in the eastern plateau (Figure 10i,j), and the Rlu value reaches its maximum at 14:00, and there are large value areas of Rlu in the eastern and southwestern plateau, and Rlu value can reach more than  $400 \text{ W/m}^2$  in the eastern part. At 20:00, the Rlu decreases and is mainly above  $350 \text{ W/m}^2$  in the eastern plateau.



**Figure 10.** Spatial distribution of LE (a–d), H (e–h), and Rlu (i–l) for four time periods in June (unit:  $\text{W/m}^2$ ).

Figure 11 shows the latitudinal profile of w, from which we can obtain that the w in the eastern plateau is larger than that in the western plateau. At 02:00 (Figure 11a), the w in the eastern plateau is larger than that in the western plateau, and it is mainly ascending motion, with the maximum value of w up to  $0.12 \text{ Pa/s}$  or more, and the area of large value of w is mainly between 600 and 300 hPa. At 08:00 (Figure 11b), the w in the western plateau becomes smaller, and a sinking motion occurs. The w in the eastern plateau continues to increase, but the vertical range becomes smaller, mainly concentrated between 600 and 400 hPa. At 14:00 (Figure 11c), the w reaches the maximum in the eastern plateau, which is about  $0.18 \text{ Pa/s}$ , and both the lateral and vertical ranges of w become larger. At 20:00 (Figure 11d), the w in the eastern plateau decreases compared to that in the afternoon, while the w in the central plateau increases, and the w is smaller and shows a sinking motion in the western plateau.



**Figure 11.** Latitudinal profiles of  $w$  at four times in June (here, positive  $w$  means rising, negative means sinking, unit: Pa/s).

### 3.2.3. Relationship between Surface Heating Field (LE and H), Rlu, $w$ , and ABLH

Table 4 shows the R of the surface heating field, Rlu, and ABLH at the three stations. It can be seen that the R of LE and H at Sieshan station passed the significance test, indicating that the significant change of ABLH is mainly due to the influence of LE and H at Sieshan station, among which the correlation between LE and ABLH was higher. The most significant effect of H on the ABLH is found at SETORS. The correlation between Rlu and ABLH is higher at Qumalai station. The correlation between  $w$  and ABLH is not high in three stations, among which the correlation between  $w$  and ABLH is highest in Sieshan station, and the other two stations do not pass the significance test.

**Table 4.** R of surface heating field, Rlu,  $w$ , and ABLH (\* indicates passing the significance test of 0.05).

ABLH	Variables				
	LE	H	Rlu	$w$	
Sieshan	0.69 *	0.66 *	0.67 *	0.52 *	
SETORS	0.83 *	0.86 *	0.82 *	0.07	
Qumalai	0.63 *	0.53 *	0.75 *	0.16	

Table 4 also shows that surface latent heat, sensible heat, and net radiation have the highest correlation with the ABLH at the SETORS station. This is because the dense vegetation releases a significant amount of latent heat during evapotranspiration, which raises the surrounding air temperature, aiding in convection development. This convection transports warm air upward, increasing the ABLH. At Sieshan Station in the cropland area, vertical velocity has the most significant impact on boundary layer height, possibly due to local circulations formed by complex terrain elevating the boundary layer height, with latent and sensible heat contributions being less dominant factors.

Figure 12 shows the daily variation of LE, H, and ABLH. It can be seen from the figure that LE and H increase at sunrise and decrease at sunset and reach the maximum value at 14:00, when the ABLH is also the highest. The LE is larger than H throughout the day and the peak difference is the largest at Sieshan station, and the peak LE is the largest among the three sites, reaching  $300 \text{ W/m}^2$  (Figure 12a). The LE at night is comparable to H or even slightly greater than the LE at SETORS, and the peak LE is the smallest among the three stations, which is about  $200 \text{ W/m}^2$  (Figure 12b). The peak H at Qumalai station is the largest among the three stations, reaching about  $140 \text{ W/m}^2$ . Under the effect of both LE and H, the heat exchange between the surface and the atmosphere is frequent, which promotes the development of ABLH (Figure 12c). The daily variation process of Rlu is basically consistent with LE and H, increasing at sunrise and decreasing at sunset, reaching the maximum at 14:00. Among the three stations, the daily variation of Rlu is obvious at Qumalai station; fluctuations are large (Figure 12c), followed by SETORS (Figure 12b), and there is least variation at Sieshan station (Figure 12a), it can be seen that

Rlu by solar radiation changes have a greater impact at Qumalai station. The Rlu heats up the atmosphere and contributes to the development of ABLH.

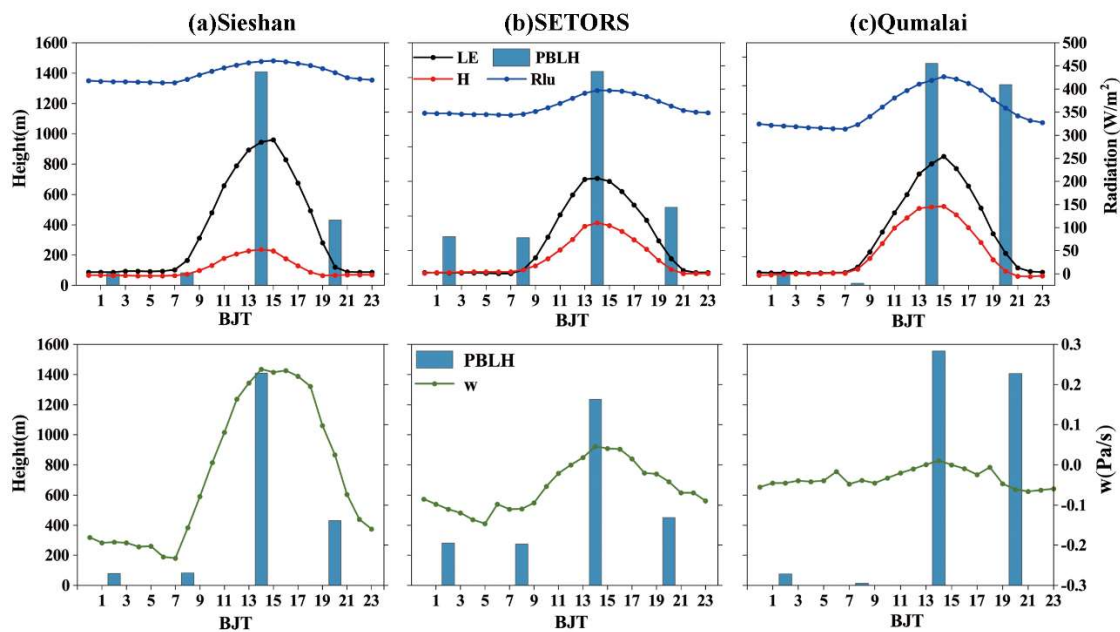


**Figure 12.** Average daily variation processes of LE, H, Rlu, w, and ABLH (top: LE, H, Rlu, and ABLH, bottom: w and ABLH) (The 3 subfigures of a–c share a common legend).

w is the component of velocity in the lead direction; in this paper, a positive w indicates upward motion, and a negative one indicates downward motion. Figure 12 shows the average daily variation of w and ABLH, and the w in this paper is taken as the value of the layer closest to the surface at the three stations. It can be seen from the figure that the w is negative in the morning and evening, when the air makes a downward motion and reaches the maximum value at each station around 14:00 when the air makes an upward motion, which is favorable to the development of ABLH. The daily variation of w at Sieshan station is basically consistent with the daily variation of ABLH (Figure 12a), which indicates that w has an effect on ABLH, while it has less effect at SETORS (Figure 12b) and almost no effect at Qumalai station (Figure 12c).

#### 4. Conclusions

Based on sounding observations and ERA5 reanalysis data from the Qumalai station and SETORS in the eastern part of the TP and the Sieshan station located at the southeastern edge of the TP in June 2022 of the Second Tibetan Plateau Scientific Expedition and Research on the TP, this paper studied the characteristics of ABLH on different underlying surfaces in the eastern TP and the influencing factors of ABLH, and reached the following conclusions:

- (1) Compared with the microwave radiometer data, the temperature difference is not obvious, and there are obvious temperature inversion phenomena in the lower layer of the observed data at Sieshan station. For the water vapor density, the difference between the four times microwave radiometer data is large, but the difference between the observed data is small at Sieshan station. The relative humidity of Sieshan station increases with height, while that increases with height and then decreases at SETORS and Qumalai station, reaching a maximum of 2200 m. The specific humidity near the ground at Qumalai station is the smallest, and the distribution of water vapor in the ABL is less. The wind direction above 2000 m is southerly or southwesterly, and the wind speed is mainly 4–8 m/s at Sieshan station. The wind direction above 1200 m is mainly southerly or southwesterly, and the wind speed changes slowly at this time at SETORS. The wind direction below 1800 m at Qumalai station is mainly southeast

- wind, and the wind direction above 1800 m gradually changes to southwest wind or westerly wind, with the maximum wind speed up to 20 m/s.
- (2) The ABL type is mainly CBL except for 14:00 at Sieshan station, and SBL at other times. The mean ABLH is 499.59 m at Sieshan station. The ABL type is mainly CBL, and the average ABLH is 560.11 m at SETORS. The ABL type is mainly CBL at 14:00 and 20:00, and SBL at other times at Qumalai station. The average height of boundary layer is 762.89 m at Qumalai station.
  - (3) The mean ABLH of the ERA5 reanalysis data in the morning and evening is smaller than observed data at Sieshan station and SETORS, whereas the opposite trend is observed at noon. At Qumalai station, the mean ABLH of the ERA5 reanalysis data in the morning and evening is larger than the observed data, with no significant differences at noon.
  - (4) In summer, the LE and H in the eastern plateau are less than those in the western plateau at 20:00, and the LE and H in the eastern plateau are greater than those in the western plateau at other three times. Rlu is greater in the eastern plateau than those in the western plateau at 02:00 and 08:00, and the opposite is true at 14:00 and 20:00. The w in the eastern plateau is greater than that in the western plateau. The diurnal variation of w in the eastern plateau is obvious, increasing first and then decreasing, mainly for upward motion.
  - (5) The influence of the surface heating field on the ABLH is most significant at Sieshan station and SETORS, while the ABLH is also influenced by the w at Sieshan station, and the ABLH is influenced by the Rlu at Qumalai station. All four influencing factors show a positive correlation with ABLH. The LE, H, and Rlu increase at sunrise and decrease at sunset and reach the maximum at around 14:00, when the w is positive and the air makes upward movement, prompting the development of ABLH.

The characteristics of the ABLH on different underlying surface types in the QTP can be summarized as follows:

**Grassland:** Grassland underlying surfaces are typically located in plateau areas with relatively flat terrain. During the day, warm surface temperatures increase the ABLH, while cold surface temperatures at night decrease it. Due to significant surface temperature variations, the boundary layer height experiences a large range of fluctuations, and it is relatively stable as it is less influenced by solar radiation and terrain.

**Forest:** The ABLH in forested areas is generally lower. This is because dense vegetation reduces direct solar radiation reaching the surface, resulting in lower surface temperatures. This, in turn, reduces the temperature gradient in the lower part of the atmospheric boundary layer, limiting its upward extent. Dense vegetation also increases surface roughness, slowing down vertical diffusion and contributing to a lower boundary layer height.

**Cropland Areas:** Underlying surfaces in mountainous cropland areas are relatively flat, with weaker solar radiation and lower vegetation cover. As a result, the boundary layer height falls between that of forests and grasslands. The increase in surface temperature is not as intense, leading to a relatively stable atmospheric boundary layer height.

The influence of different underlying surface types on the ABLH is primarily reflected in surface temperature variations, solar radiation intensity, vegetation cover, and terrain. Grasslands typically exhibit a larger range of boundary layer height variations, while forests and mountainous agricultural areas are relatively stable.

**Author Contributions:** Conceptualization, X.W., methodology and writing, J.M., formal analysis and validation, M.C. All authors have read and agreed to the published version of the manuscript.

**Funding:** The Second Tibetan Plateau Scientific Expedition and Research Program (STEP) (grant number 2019QZKK010304). The National Natural Science Foundation of China (grant number 41975096), the Open Grants of the State Key Laboratory of Severe Weather (2023LASW-B08) and the Technological Innovation Capacity Enhancement Program of the Chengdu University of Information Technology (grant number KYQN202203) provided financial support for this study.

**Data Availability Statement:** ERA5 reanalysis data (ERA5 hourly data on single levels from 1940 to present (copernicus.eu), ERA5 hourly data on pressure levels from 1940 to present (copernicus.eu), accessed on 1 November 2022).

**Acknowledgments:** The authors thank ERA5 reanalysis data from the ECMWF for providing support for this study.

**Conflicts of Interest:** The authors declare no conflicts of interest.

## References

1. Su, Y.; Lü, S.; Fan, G. The characteristics analysis on the summer atmospheric boundary layer height and surface heat fluxes over the Qinghai-Tibetan Plateau. *Plateau Meteorol.* **2018**, *37*, 1470–1485.
2. Stull, R.B. *An Introduction to Boundary Layer Meteorology*; Springer Science & Business Media: Berlin/Heidelberg, Germany, 1988; Volume 13.
3. Li, Y.; Hu, Z.; Zhao, H. Overview on the Characteristic of Boundary Layer Structure in Tibetan Plateau. *Plateau Mt. Meteorol. Res.* **2012**, *32*, 91–96.
4. Wan, Y.; Zhang, Y.; Zhang, J.; Peng, Y. Influence of sensible heat on planetary boundary layer height in East Asia. *Plateau Meteorol.* **2017**, *36*, 173–182.
5. Baklanov, A.A.; Grisogono, B.; Bornstein, R.; Mahrt, L.; Zilitinkevich, S.S.; Taylor, P.; Larsen, S.E.; Rotach, M.W.; Fernando, H.J.S. The Nature, Theory, and Modeling of Atmospheric Planetary Boundary Layers. *Bull. Am. Meteorol. Soc.* **2011**, *92*, 123–128. [[CrossRef](#)]
6. Zhang, Q.; Zhang, J.; Qiao, J.; Wang, S. Relationship of atmospheric boundary layer depth with thermodynamic processes at the land surface in arid regions of China. *Sci. China Earth Sci.* **2011**, *54*, 1586–1594. [[CrossRef](#)]
7. Zhao, M. A Review of the Research on the Effects of Boundary Layer and Land Surface Process on Heavy Rain in China. *Torrential Rain Disasters* **2008**, *2*, 186–190.
8. Ma, Y.; Hu, Z.; Wang, B.; Ma, W.; Chen, X.; Han, C.; Li, M.; Zhong, L.; Gu, L.; Sun, F.; et al. The Review of the Observation Experiments on Land-Atmosphere Interaction Progress on the Qinghai-Xizang (Tibetan) Plateau. *Plateau Meteorol.* **2021**, *40*, 1241–1262.
9. Xu, G.; Cui, C.; Zhou, Z.; Zhang, B.; Li, Y.; Zhao, X. Atmospheric boundary layer heights estimated from radiosonde observations over the Qinghai-Tibet Plateau and its downstream area. *Torrential Rain Disasters* **2014**, *33*, 217–227.
10. Fu, W.; Li, M.; Yin, S.; Lü, Z.; Wang, L.; Shu, L. Study on the Atmospheric Boundary Layer Structure of the Qinghai Xizang Plateau under the South Branch of the Westerly Wind and the Plateau Monsoon Circulation Field. *Plateau Meteorol.* **2022**, *41*, 190–203.
11. Song, X.; Zhang, H.; Liu, X.; Fan, S.; Liu, H.; Hu, F.; Li, S.; Zhou, M.; Bian, L.; Xu, X. Determination of atmospheric boundary layer height in unstable conditions over the middle Tibetan Plateau. *Acta Sci. Nat. Univ. Pekin.* **2006**, *42*, 328–333. [[CrossRef](#)]
12. Jiang, X.; Li, Y.; He, G. The climatic characteristics analysis of radiosonde data over east part of Tibetan Plateau. *Plateau Mt. Meteorol. Res.* **2008**, *28*, 1–9.
13. Li, M.; Ma, Y.; Hu, Z.; Ma, W.; Wang, J.; Ogino, S.-Y. Study on characteristics of atmospheric boundary layer over Naqu region of Northern Tibetan Plateau. *Plateau Meteorol.* **2004**, *23*, 728–733.
14. Li, M.; Dai, Y.; Ma, Y.; Zhong, L.; Lü, S. Analysis on structure of atmospheric boundary layer and energy exchange of surface layer over Mount Qomolangma region. *Plateau Meteorol.* **2006**, *25*, 807–813.
15. Li, M.; Ma, Y.; Ma, W.; Ishikawa, H.; Sun, F.; Ogino, S.-Y. Structural difference of atmospheric boundary layer between dry and rainy seasons over the central Tibetan Plateau. *J. Glaciol. Geocryol.* **2011**, *33*, 72–79.
16. Ma, W.; Dai, Y.; Ma, Y.; Hu, Z.; Li, M.; Wang, J. Analysis on the boundary layer and spatial profile of northern Tibetan Plateau area by radiosonde data. *J. Arid. Land Resour. Environ.* **2005**, 40–46.
17. Gu, L.; Hu, Z.; Lü, S.; Yao, J. Atmosphere Boundary Layers in Typical Days over the North Tibet Plateau during Summer. *J. Glaciol. Geocryol.* **2006**, 893–899.
18. Wang, S.; Ma, Y. The structure of atmospheric boundary Layer over mount Qomolangma in summer. *J. Glaciol. Geocryol.* **2008**, *30*, 681–687.
19. Chen, X.; Škerlak, B.; Rotach, M.W.; Añel, J.A.; Su, Z.; Ma, Y.; Li, M. Reasons for the extremely high-ranging planetary boundary layer over the western Tibetan Plateau in winter. *J. Atmos. Sci.* **2016**, *73*, 2021–2038. [[CrossRef](#)]
20. Li, W.; Xing, Y.; Ma, S. The analysis and comparison between GTS1 radiosonde made in China and RS92 Radiosonde of Vaisala company. *Meteorol. Mon.* **2009**, *35*, 97–102.
21. Ran, Y.; Li, X.; Lu, L. China Land Cover Classification at 1 km Spatial Resolution Based on a Multi-source Data Fusion Approach. *Adv. Earth Sci.* **2009**, *24*, 192–203.
22. Hersbach, H.; Bell, B.; Berrisford, P.; Horányi, A.; Sabater, J.M.; Nicolas, J.; Radu, R.; Schepers, D.; Simmons, A.; Soci, C. Global reanalysis: Goodbye ERA-Interim, hello ERA5. *ECMWF Newsl.* **2019**, *159*, 17–24.
23. Eresmaa, N.; Karppinen, A.; Joffe, S.; Räsänen, J.; Talvitie, H. Mixing height determination by ceilometer. *Atmos. Chem. Phys.* **2006**, *6*, 1485–1493. [[CrossRef](#)]
24. Seibert, P.; Beyrich, F.; Gryning, S.-E.; Joffe, S.; Rasmussen, A.; Tercier, P. Review and intercomparison of operational methods for the determination of the mixing height. *Atmos. Environ.* **2000**, *34*, 1001–1027. [[CrossRef](#)]

25. Yang, F. Comparison of Determination Methods and Characteristics of Boundary Layer Height in Semi-Arid Area. Master's Thesis, Lanzhou University, Lanzhou, China, 2018.
26. Yang, F. The Atmospheric Boundary Layer Height Study Based on Ground-Based Remote Sensing and Numerical Simulation. Master's Thesis, Nanjing University, Nanjing, China, 2015.
27. Holzworth, G.C. Estimates of mean maximum mixing depths in the contiguous United States. *Mon. Weather. Rev.* **1964**, *92*, 235–242. [[CrossRef](#)]
28. Holtslag, A.; De Bruijn, E.; Pan, H. A high resolution air mass transformation model for short-range weather forecasting. *Mon. Weather. Rev.* **1990**, *118*, 1561–1575. [[CrossRef](#)]
29. Sicard, M.; Pérez, C.; Rocadenbosch, F.; Baldasano, J.; García-Vizcaino, D. Mixed-layer depth determination in the Barcelona coastal area from regular lidar measurements: Methods, results and limitations. *Bound.-Layer Meteorol.* **2006**, *119*, 135–157. [[CrossRef](#)]
30. Zhang, Q.; Wang, S. A study on atmospheric boundary layer structure on a clear day in the arid region in northwest China. *Acta Meteorol. Sin.* **2008**, 599–608.

**Disclaimer/Publisher's Note:** The statements, opinions and data contained in all publications are solely those of the individual author(s) and contributor(s) and not of MDPI and/or the editor(s). MDPI and/or the editor(s) disclaim responsibility for any injury to people or property resulting from any ideas, methods, instructions or products referred to in the content.